# Discontinuous thinning in active microrheology of soft complex matter

R. Wulfert,[1] U. Seifert,[1] and T. Speck[2]

[1]*II. Institut für Theoretische Physik, Universität Stuttgart, Pfaffenwaldring 57, 70550 Stuttgart, Germany*

[2]*Institut für Physik, Johannes Gutenberg-Universität Mainz, Staudingerweg 7-9, 55128 Mainz, Germany*

(Received 17 February 2016; revised manuscript received 28 September 2016; published 27 December 2016)

Employing theory and numerical simulations, we demonstrate discontinuous force thinning due to the driven motion of an external probe in a host medium. We consider two cases: an ideal structureless medium (modeling ultrasoft materials such as polymer melts) and a dilute bath of interacting repulsive particles. When the driving of the probe exceeds a critical force, the microviscosity of the medium drops abruptly by about an order of magnitude. This phenomenon occurs for strong attractive interactions between a large probe and a sufficiently dense host medium.

DOI: 10.1103/PhysRevE.94.062610

## I. INTRODUCTION

Active microrheology (AMR) is an experimental technique to determine local rheological properties of complex environments by tracing actively manipulated probes (for reviews see, e.g., Refs. [1–3]). For colloidal suspensions, it has been employed close to the glass transition by dragging a magnetic bead [4], for hard spheres over a wide range of volume fractions [5], and to force the local melting of a colloidal crystal [6,7]. It has also become an important technique for the study of mechanical properties of biological matter [8,9] and fluid interfaces [10]. Moreover, it allows quantitative insights into the mechanical response of glassy materials [11–14] and crowded systems [15].

An established theoretical model for AMR is the "simple paradigm" of Squires and Brady [16,17], which has been applied predominantly to hard-sphere suspensions. It allows us to describe a broad class of materials governed by short-ranged repulsions through a mapping onto hard spheres via an effective diameter. Conventional macrorheology deals with averages of quantities like stress and strain, which requires sample materials to be both sufficiently homogeneous and spatially extended. In AMR, however, the host medium is strained only in the vicinity of the moving probe. It is this locality of the induced flow fields that makes AMR so useful for the exploration of media that are either confined (e.g., in living cells), heterogeneous on mesoscopic length scales, or just difficult to procure in larger quantities. Like macrorheology, AMR centers around measuring and understanding the non-Newtonian behavior of complex fluids, albeit from a more introversive angle. This predominantly concerns their relaxation in response to perturbations [18,19] as well as their thinning and thickening behavior under steady flows [20,21]. To this end, the simple paradigm relates changes in the microstructure to microrheological properties.

Of particular importance are materials with discontinuous flow curves. Such discontinuities give rise to rather spectacular effects, a paradigmatic example being the sudden solidification of cornstarch suspensions above some critical strain rate. Although the phenomenon of discontinuous shear thickening [22] has long been known, its underlying mechanism remains the subject of ongoing theoretical and experimental investigations [23–25]. The opposite case, discontinuous shear thinning, has received far less attention and so far has only been reported in connection with order-disorder transitions under shear flow [26,27].

Here we report the discontinuous thinning of a soft material in response to the motion of a forced probe *attracting* the surrounding host material. A numerical analysis based on an extension of the simple paradigm formalism [16] reveals a dynamically unstable regime within the velocity-force relation of the driven probe. We corroborate our results with Brownian dynamics simulations showing that, given sufficient density and attraction strength, crossing a certain threshold in the driving force induces a marked discontinuous drop in the microviscosity of the host medium. Moreover, for finite-time force protocols across this discontinuity, the dynamic lag of the microstructure causes hysteretic behavior, showing up as a loop in the corresponding flow curves. The underlying mechanism of this discontinuous force thinning turns out to be rather generic and intuitive. It can be accounted for solely in terms of microstructure, i.e., the aggregation of bath particles around the probe due to attraction and how this aggregation is affected by the advection at increasing probe velocities. We also discuss the impact of bath particle interactions on the instability and establish a parameter range in terms of volume fraction and relative particle size where our results extend to hard-sphere bath particles.

## II. MODEL

We model the host medium as $N$ bath particles with hydrodynamic diameter $b$ suspended in a solvent and moving in a periodic box of volume $V$ (number density $\rho \equiv N/V$). A spherical probe of diameter $a$ is pulled through the bath by a constant external force $f\mathbf{e}_x$. Interparticle forces $\mathbf{F}_k = -\boldsymbol{\nabla}_k U$ are derived from the superposition $U = U(\{\mathbf{x}_k\})$ of pair potentials $u(r)$ and $u_b(r)$, acting between the probe and bath particles and among bath particles, respectively. Throughout, we measure lengths in units of $a$, energies in $k_\mathrm{B}T$, and diffusivity in $(D_a+D_b)$, which is the relative diffusivity between the probe and bath particles. The solvent is assumed to be Newtonian with a viscosity $\eta$ large enough to render the colloidal inertia irrelevant. The resulting Brownian motion generates particle trajectories $\mathbf{x}_k(t)$ described by the overdamped Langevin equations,

$$\dot{\mathbf{x}}_k = \mu_k[\mathbf{F}_k + f\mathbf{e}_x\delta_{0k}] + \boldsymbol{\zeta}_k, \tag{1}$$

 

with $k = 0$ referring to the probe. The noise $\boldsymbol{\zeta}_k(t)$ has zero mean and correlations $\langle \boldsymbol{\zeta}_k(t) \otimes \boldsymbol{\zeta}_l(t') \rangle = 2\mu_k \delta_{kl} \mathbf{I} \delta(t - t')$ with identity matrix $\mathbf{I}$. Stokes' law of friction for spherical particles yields (in our units) the mobilities $\mu_0 = b/(1 + b)$ and $\mu_{1\ldots N} = 1/(1 + b)$ of probe and bath particles with the (relative) bath particle size $b$.

An equivalent description is given in terms of the joint probability distribution $\Psi(\{\mathbf{x}_k\},t)$ with local mean velocities $\mathbf{v}_k = \mu_k(\mathbf{F}_k + f\,\mathbf{e}_x \delta_{0k} - \boldsymbol{\nabla}_k \ln \Psi)$. After switching to bath coordinates relative to the probe, $\{\mathbf{r}_{k=1..N} \equiv \mathbf{x}_k - \mathbf{x}_0\}$, all gradients with respect to the absolute position $\mathbf{x}_0$ of the probe vanish due to the homogeneity of the system. Conservation of probability amounts to the many-body Smoluchowski equation, which in the stationary case reads

$$\sum_{k=1}^{N} \boldsymbol{\nabla}_k \cdot (\mathbf{v}_k - \mathbf{v}_0) \Psi_s = 0. \tag{2}$$

It determines the nonequilibrium steady-state distribution $\Psi_s(\{\mathbf{r}_k\}; f)$, which includes the microstructural deformations induced by the external driving. Unless stated otherwise, averages $\langle \cdot \rangle$ are taken with respect to $\Psi_s$. For pairwise interactions the mean frictional drag,

$$\rho\zeta(f) \equiv \mathbf{e}_x \cdot \langle \mathbf{F}_0 \rangle_f = \rho \int \mathrm{d}\mathbf{r}\, (\mathbf{e}_x \cdot \mathbf{e}_r)\, u'(|\mathbf{r}|)\, g(\mathbf{r}; f), \tag{3}$$

exerted on the probe reduces to an integral involving the one-body density $\rho_1(\mathbf{r}; f) = \rho g(\mathbf{r}; f)$ of bath particles around the probe with conditional probability $g(\mathbf{r}; f)$ to find a bath particle at $\mathbf{r}$ given the probe at the origin. In general, this density will depend both on the driving strength $f$ and bath density $\rho$. The ensuing velocity-force relation,

$$\overline{v}(f) \equiv \mathbf{e}_x \cdot \langle \mathbf{v}_0 \rangle_f = \mu_0 [f - \rho\zeta(f)], \tag{4}$$

expresses the nonlinear response of the probe to the external driving, reducing the solution of the microrheological problem to the calculation of $g(\mathbf{r}; f)$.

The one-body density $\rho_1(\mathbf{r})$ is the first member of an open hierarchy of conditional densities. In order to achieve closure, we approximate the two-body density $\rho_2(\mathbf{r}, \mathbf{r}') \approx \rho_1(\mathbf{r})\rho_1(\mathbf{r}')$, thereby neglecting *any* correlations between bath particles. For strongly interacting particles, such an approximation would correspond to the dilute limit. However, for now we use it as a model for structureless soft media at arbitrary density such as polymer melts with probe sizes larger than the microscopic correlation length [28]. Within this approximation, we obtain the pair-Smoluchowski equation,

$$\boldsymbol{\nabla} \cdot [\boldsymbol{\nabla} + \overline{v}\mathbf{e}_x + u'(|\mathbf{r}|)\mathbf{e}_r] g(\mathbf{r}; \overline{v}) = 0, \tag{5}$$

which is essentially the constitutive equation of the simple paradigm [16], including continuous pair interactions $u(r)$ between probe and bath particles. Equation (5) has the form of an advection-diffusion equation with $\overline{v}$ quantifying the advection of bath particles as seen from the moving probe, which is of course equal in magnitude to the mean probe velocity in the laboratory frame. In the units chosen above, $\overline{v}$ is the Peclet number commonly used to quantify the relative strength of advection versus diffusivity [16]. Note, however, that we do not follow the simple paradigm in replacing $\overline{v}$ with $\mu_0 f$ in Eq. (5), which is admissible only in the dilute limit $\rho \to 0$, but rather continue with an alternative way to solve the microrheological problem. Solving Eq. (5) yields $g(\mathbf{r}; \overline{v})$ as a function of the mean velocity $\overline{v}$ *independent* of density $\rho$, rendering the particle drag $\rho\zeta(\overline{v})$ strictly linear in $\rho$. From Eq. (4) then follows the force $f(\overline{v}) = \rho\zeta(\overline{v}) + \overline{v}(f)/\mu_0$ necessary to balance the total drag (right-hand side) at a given mean velocity $\overline{v}$. The above considerations comprise the constant-force case of microrheology, as opposed to the constant-velocity case, both extensively discussed in the simple paradigm [16]. However, in order to arrive at the constant-velocity case, where the probe moves deterministically at some fixed velocity $v_c$, the only necessary adjustments are the replacement of $\overline{v} \to v_c$ in Eq. (5), while changing the unit of diffusivity to $D_b$.

Whereas in the hard-sphere case an analytical solution to Eq. (5) is available in the form of a series expansion [16], here we have to resort to a numerical scheme. To solve Eq. (5), with the axial symmetry around the force direction taken into account, we employ spherical coordinates and expand $g(r,\theta)$ into Legendre polynomials. Discretizing the modes with respect to $r$ leads to a system of linear equations, which is solved by standard techniques. After having sampled the microrheological flow curve with a sufficient number of value pairs $(\overline{v}, f)$, the $f(\overline{v})$ relation can be numerically interpolated and inverted to give the desired $\overline{v}(f)$ velocity-force relation for given density $\rho$.

## III. RESULTS

### A. Ideal bath

For the probe-bath interactions we choose the Lennard-Jones (LJ) potential

$$u(r) = 4\epsilon \left[ \left(\frac{\sigma}{r}\right)^{12} - \left(\frac{\sigma}{r}\right)^{6} \right], \tag{6}$$

which combines attraction with a steep repulsive inner part. In the case of a passive probe, i.e., $f = 0$, the isotropic equilibrium distribution of bath particles is $g_{\mathrm{eq}}(r) = \exp[-u(r)]$. Driving the probe with finite $f$ breaks isotropy and leads to a characteristic, predominantly dipolar microstructural deformation. For rather high interaction strength $\varepsilon = 5$ and length scale $\sigma = 1$ of the LJ potential, Figs. 1(a)–1(d) depict the evolution of $g(\mathbf{r}; \overline{v})$ with increasing probe drift velocity $\overline{v}$. In the case of a slowly moving probe [Fig. 1(a)] the potential well is still highly populated with bath particles, while the region of maximal excess is shifted downstream due to advection. Naturally, dragging along these trailing particles generates considerable frictional resistance against the probe drift. Upstream, suction toward the potential minimum creates a halo-like region of depleted bath density. With increasing drift velocity $\overline{v}$, the directional bias in the microstructure becomes more and more pronounced, see Figs. 1(b) and 1(c). As bath particles now have less time to react to the potential forces while passing the probe, its upstream range of influence contracts radially. Meanwhile, the probe trails behind it a wake of ever-increasing spatial dilation. Although this wake is still carrying an excess of bath particles, its peak density is reduced. When the drift becomes strong enough, however, advection dominates over the attractive potential forces and

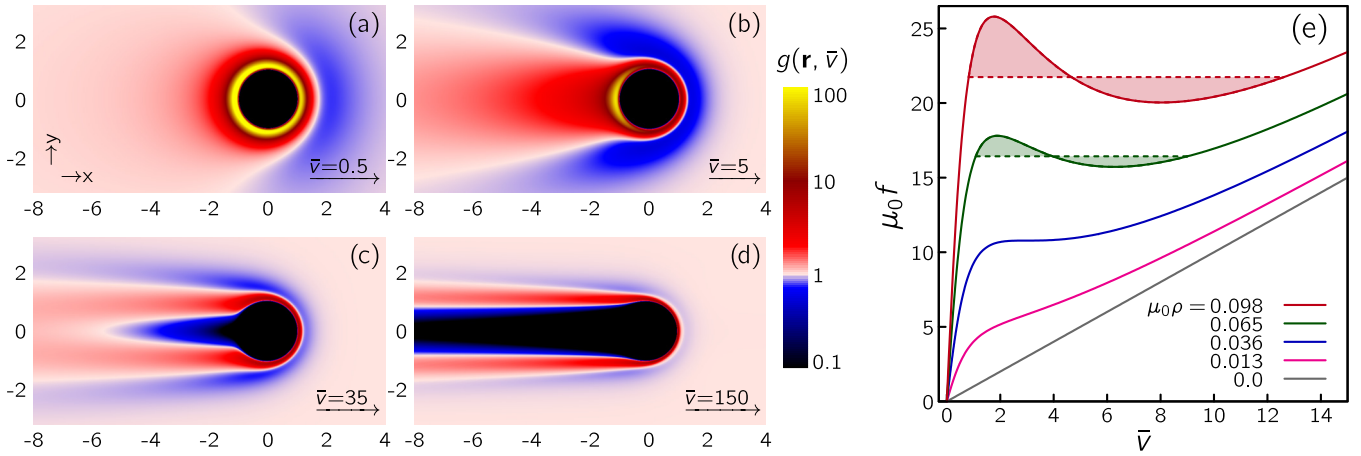


FIG. 1. (a–d) Microstructural deformation around the attractive probe for increasing mean velocities $\overline{v}$ in terms of the conditional probability $g(\mathbf{r};\overline{v})$ in the $x$-$y$ plane. Probe and bath particles interact via a Lennard-Jones potential with $\varepsilon = 5$ and $\sigma = 1$. (e) Velocity-force relations $\mu_0 f(\overline{v})$ for ascending values of $\mu_0\rho$ (bottom to top) at a relative bath particle size $b = 1/19$. Above $\mu_0\rho \simeq 0.036$, the flow curves become nonmonotonous and dynamically unstable regions emerge across intermediate $\overline{v}$. Dashed lines and shaded areas represent a tentative equal-area Maxwell construction to restore invertibility.

the downstream excess starts being swept away, resulting in a more or less evacuated tail-like zone directly behind the probe; see Fig. 1(c). Having cast off its "baggage," the probe can now propagate much more freely. It is only for very strong driving that the distribution of bath particles starts to resemble the typical hard-sphere picture [Fig. 1(d)], where regardless of driving strength one observes a buildup of particles in front of the probe and a depleted wake trailing it.

The velocity-force relations corresponding to this intriguing, highly nonlinear behavior are depicted in Fig. 1(e). Plotting $\mu_0 f$ versus the average probe velocity $\overline{v}$ leaves $\mu_0\rho = \rho b/(1+b)$ as the only free parameter; cf. Eq. (4). The most salient feature in Fig. 1(e) is that upon increasing the density $\rho$ for constant $b$, here specifically above $\mu_0\rho \simeq 0.036$, the flow curves become nonmonotonous over an intermediate $\overline{v}$-range. This implies that the probe requires less forcing in order to travel faster, which clearly constitutes a dynamically unstable regime. At the same time, the function $f(\overline{v})$ is no longer globally invertible. Since the force $f$ is the physical control parameter, and stochastic dynamics guarantees a unique steady state with an unambiguous drift velocity $\overline{v}$, this implies a discontinuous change of the velocity-force relation $\overline{v}(f)$.

Nonmonotonous flow curves have been found to model, e.g., shear banding [29,30] and shear thickening [24]. In conventional thermodynamics such a behavior signals a phase transition. For example, in the van der Waals theory the volume as a function of pressure shows a similar loop due to the competition between energy (favoring the dense phase) and entropy (favoring the dilute phase). The Maxwell construction replaces the loop by an isobar equating the free energies of both phases. We note the analogy between intensive pressure and force, and extensive volume and the distance traveled by the probe. As a for now purely tentative measure to restore invertibility, we propose, in the spirit of a Maxwell construction, that the unstable sinusoidal part of $f(\overline{v})$ ought to be replaced by a horizontal line as shown in Fig. 1(e).

In order to assess the physical validity of the resulting flow curves, we have performed Brownian dynamics simulations. In contrast to solving Eq. (5) for given $\overline{v}$, we now control the driving force $f$ directly, allowing us to sample the true $\overline{v}(f)$ relations over the critical region. There is, however, a subtle discrepancy with respect to the ideal bath model: In simulations, even for noninteracting bath particles with $u_b(r) = 0$, we cannot trivially rule out any bath correlations as in the pair-Smoluchowski approach, since there is the possibility of indirect correlations mediated by the probe. It turns out, however, that in the case of small bath particles $b \ll 1$ these correlations become negligible and the two approaches converge.

For $N = 32\,000$ particles with relative size $b = 1/19$ plus the probe, trajectories $\mathbf{x}_k(t)$ are integrated according to a time-discretized Euler scheme based on Eq. (1) with a time step $\Delta t = 10^{-4}$. The system is allowed for $\tau_{\rm rel} = 100$ to relax toward its nonequilibrium steady state prior to collecting any data. An estimate of the mean probe velocity $\overline{v}(f)$ is then obtained as an average over 10 statistically independent runs per given force $f$, corresponding to an average $\langle\cdot\rangle$ with respect to the noise $\{\boldsymbol{\zeta}_k(t)\}$. Each run has a duration of $\tau_{\rm sim} = 200$, which is roughly how long it would take for an isolated bath particle to spread diffusively by roughly 34 probe diameters.

Introducing terminology from microrheology, we consider the relative microviscosity $\eta_{\rm mrh}/\eta \equiv \mu_0 f/\overline{v}$. Its definition hypothesizes a Newtonian medium of the same viscosity, whose purely Stokesian resistance to the probe equals the total friction $(\overline{v}/\mu_0 + \rho\zeta)$ in the suspension. In contrast to a Newtonian viscosity, however, the microviscosity $\eta_{\rm mrh}$ of complex fluids will generally be a function of $\overline{v}$ or $f$, respectively, just as the macroscopic shear viscosity will be a function of strain rate or stress. The relative microviscosity $\eta_{\rm mrh}/\eta$ as a function of driving force $f$ is shown in Fig. 2(a) both for the Brownian dynamics simulations and the solution of Eq. (5). In the stable case with $\mu_0\rho = 0.036$ the two methods match almost perfectly. Pronounced but continuous thinning takes place over an intermediate force range, with the relative microviscosity declining by more than one order of magnitude, followed by an asymptotic decay with $\lim_{f\to\infty} \eta_{\rm mrh}(f)/\eta = 1$. In this strong

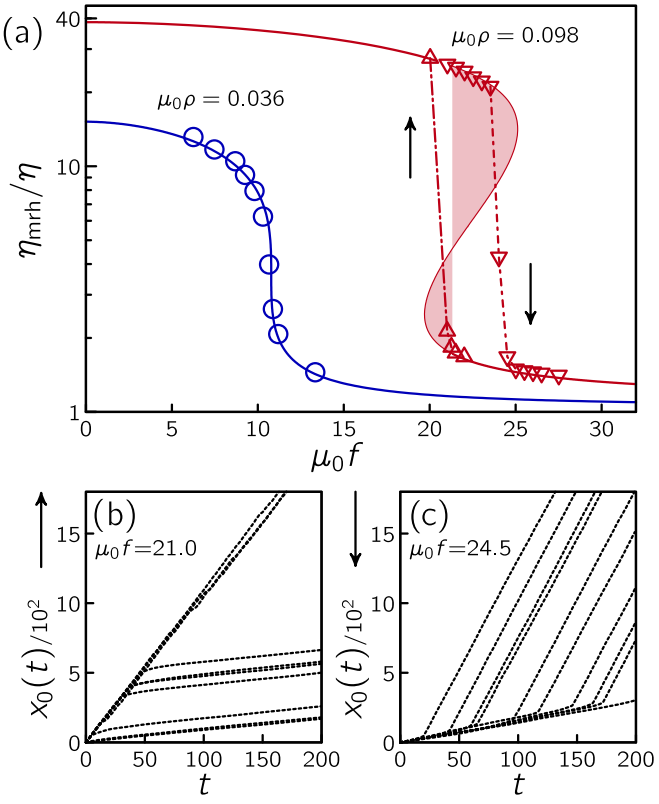


FIG. 2. (a) Relative microviscosity $\eta_{\rm mrh}/\eta = \mu_0 f/\overline{v}$ as a function of driving force $f$ for two different parameters $\mu_0\rho$. Solid lines represent numerical solutions of the pair-Smoluchowski Eq. (5). Data points from Brownian dynamics simulations with fixed $b = 1/19$ fall onto the numerical solution with statistical errors smaller than the symbol size. In the unstable case with $\mu_0\rho = 0.098$, simulations reveal a sharp discontinuous transition between two separate frictional regimes. The transition force depends on the rate and direction along which $f$ is varied (see arrows), leading to hysteretic behavior. (b, c) Individual probe trajectories $x_0(t)$ for initial forces (b) below and (c) above the discontinuity. In order to escape the metastable initial state, a rare fluctuation has to carry the system close enough toward its stable steady state, followed by a marked and abrupt shift in the probe velocity.

driving regime, where advection dominates over any pair interactions with a finite energy scale, the particle contribution $\rho\zeta$ to the total friction $(\overline{v}/\mu_0 + \rho\zeta)$ becomes increasingly irrelevant. This result is in stark contrast to the singular behavior of a hard-sphere suspension, where the microviscosity asymptotically converges to a quasi-Newtonian plateau given by $\lim_{f\to\infty} \eta_{\rm mrh}(f)/\eta - 1 = \frac{1}{2}(\eta_{\rm mrh}(0)/\eta - 1)$ [16].

Regarding the thinning behavior in the unstable case, specifically for $\mu_0\rho = 0.098$ in Fig. 2(a), Brownian dynamics simulations reveal a sharp discontinuous transition between the two frictional regimes within the unstable region. The microviscosity $\eta_{\rm mrh}/\eta$ suddenly drops (or surges) by more than one order of magnitude, depending on the rate and direction along which $f$ is varied. Here, the fact that the simulation results in Fig. 2(a) fork into two branches across the instability is due to the rather long crossover time from metastable initial states to the stable steady state. Hence, there is a difference whether the initial relaxation of the system starts with $f = 0$ and the force being slowly ramped up [see Fig. 2(c)], or whether it starts with a force beyond the unstable region, which is then gradually reduced toward its steady-state value [see Fig. 2(b)]. For finite relaxation times, this leads to hysteretic behavior around a critical force, which is compatible with the estimate from the Maxwell construction, once again represented by the shaded area in Fig. 2(a). We expect that in the limit of infinitely long simulation time, which would correspond to the true steady-state ensemble, the hysteresis will contract to a single discontinuous step at the critical force.

### B. Interacting bath particles

In a first step toward more realistic systems, we use Brownian dynamics simulations to produce flow curves of an attractive probe in suspensions where particles interact via some pair potential $u_b(r) \neq 0$. A natural way to model media with intrinsic structure, i.e., having spatial correlations, is to incorporate volume-exclusion effects by having bath particles interacting as hard spheres. Considering that the instability requires rather strong local aggregation of particles in the potential well, it is to be expected that volume exclusion effects will significantly impact the microstructure and thus also the microrheological thinning mechanism.

For numerical convenience, we approximate the singular hard-sphere interactions by a continuous, purely repulsive WCA potential,

$$u_b(r) = \begin{cases} 4\epsilon_b\left[\left(\frac{\sigma_b}{r}\right)^{12} - \left(\frac{\sigma_b}{r}\right)^{6}\right] + \epsilon_b, & r \leqslant 2^{\frac{1}{6}}\sigma_b \\ 0, & r > 2^{\frac{1}{6}}\sigma_b \end{cases}, \qquad (7)$$

where the energy scale $\epsilon_b$ and length scale $\sigma_b$ govern the repulsive stiffness and the effective size of the bath particles, respectively. In order to assess the impact of volume exclusion, we gradually increase the effective particle size from zero, the latter corresponding to the ideal-bath case studied above. To this end, it is instructive to vary $\sigma_b$ independently while fixing all other parameters that would affect the microrheological behavior. Explicitly, we choose a bath number density $\rho = 0.92$ and a hydrodynamic diameter $b = 0.1$. Regarding the probe-bath attraction, we stick to the Lennard-Jones potential from Eq. (6) with $\epsilon = 5$ and $\sigma = 1$, as utilized above.

The Brownian dynamics simulation scheme remains essentially the same as for noninteracting particles but for $N = 4000$ particles with density $\rho = 0.92$. All results have been numerically checked to be robust against an increase in $N$ within the margin of statistical errors. A time step of $\Delta t = 1 \times 10^{-6}$ ensures stable dynamics with regard to the short length scales $\sigma_b$ associated with the WCA potential. After an initial random placement of particles, the system relaxes by gradually adopting the proper probe-bath microstructure, while the force $f$ is slowly being ramped up from zero. The initial relaxation period lasts for $\tau_{\rm rel} = 20$, during the second half of which the force has reached its constant steady-state value. For each force value, 15 independent runs are performed with a duration of $\tau_{\rm sim} = 10$ each.

Simulation results are shown along with the corresponding ideal-bath results in Fig. 3 in terms of the relative microviscosity $\eta_{\rm eff}/\eta = \mu_0 f/\overline{v}$ for increasing values of $\sigma_b$. In order to allow for better recognition of discontinuous behavior, the

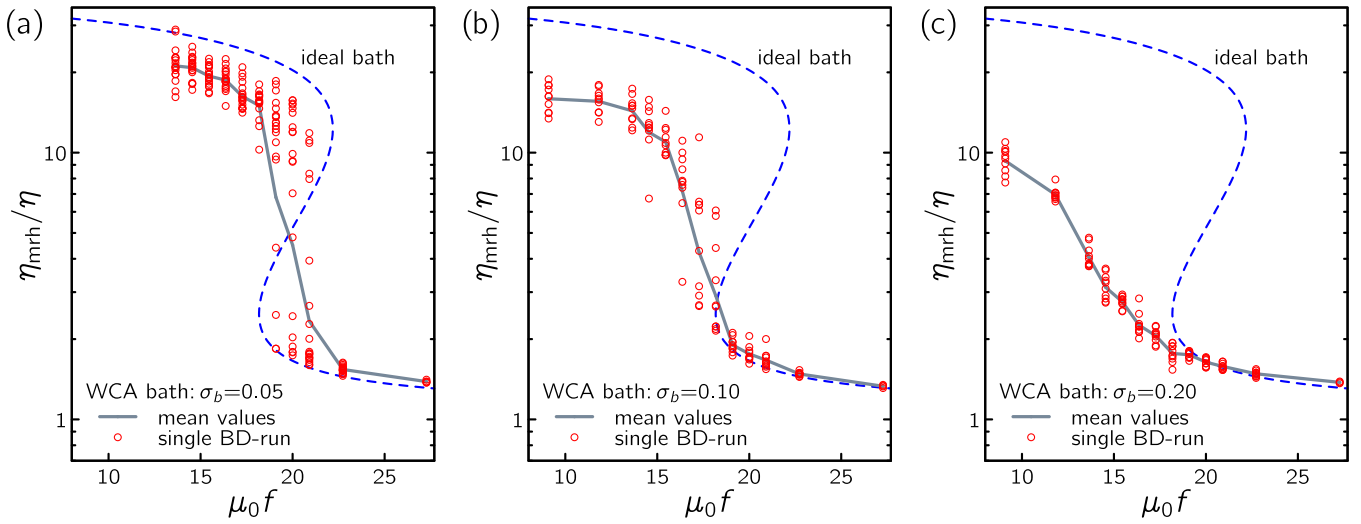


FIG. 3. Relative microviscosity $\eta_{\mathrm{mrh}}/\eta = \mu_0 f/\overline{v}$ as a function of force $f$ at fixed $\epsilon_b = 1.0$ and number density $\rho = 6\phi/(\pi b^3) = 0.92$ for increasing bath particle size in terms of the WCA-potential range $\sigma_b$: (a) $\sigma_b = 0.05$, (b) $\sigma_b = 0.10$, and (c) $\sigma_b = 0.20$. Bath particles have a relative hydrodynamic diameter $b = 0.1$ corresponding to a probe mobility of $\mu_0 = 0.091$. The flow curve according to the ideal-bath model (dashed lines) serves as a reference for the noninteracting ($\sigma_b = 0$) case.

values of $\eta_{\mathrm{eff}}/\eta$ are shown both for the mean probe velocity $\overline{v}$ averaged over single simulation runs (symbols) as well as over all trajectories pertaining to a given force $f$ (solid lines). Due to the long persistence of metastable states close to the discontinuity, simulations with a finite duration and relaxation time yield trajectories where a transition has already taken place at simulation start, some where it is still pending and some where it occurs during the simulation.

It is clear from Figs. 3(a)–3(c) that the microrheological behavior is impacted by volume exclusion among bath particles. In the weak driving regime, i.e., before major thinning occurs, the high value of $\eta_{\mathrm{eff}}/\eta$ predicted by the ideal-bath model is strongly diminished by an increase in bath particle extension $\sigma_b$. This is due to the fact that the major contribution to the microviscosity for slow driving stems from a pronounced aggregation of particles in the potential well, which is naturally counteracted by volume exclusion. As explained above, the instability is predicated upon the high initial aggregation, which is eventually flushed out of the potential well by advection, leading to a marked drop in microviscosity. The simulations demonstrate that when this aggregation is sufficiently weakened, the instability vanishes as a consequence.

In the case of a rather small $\sigma_b = 0.05$, Fig. 3(a), the discontinuity is still present, which can be inferred from the vertical spread of data points pertaining to forces across the unstable range. Most of these data points can be clearly assigned to one of two distinct frictional regimes. While this clearly shows the presence of discontinuous transitions on the trajectory level, the superposition is merely of a transient nature and due to some systems not having reached their final steady state yet. Note that the few intermediate data points do not indicate a continuous transition but rather pertain to trajectories where the crossover has occurred during simulation time, consequently yielding an average somewhere in between the two regimes. Given a sufficiently long initial relaxation period, all metastable states will eventually have transitioned into stable steady states, resulting in a clear-cut discontinuous step in the $\eta_{\mathrm{eff}}(f)/\eta$ flow curves. As $\sigma_b$ increases, the unstable behavior becomes less pronounced, Fig. 3(b), and has vanished for $\sigma_b = 0.2$ (c). Note that the strong-driving regime that follows the thinning transition turns out to be more or less unaffected by the bath interactions.

To give an idea for which parameters one can expect discontinuous force thinning, note that the microrheological behavior remains invariant for

$$\mu_0\rho = \frac{b}{1+b}\rho = \frac{6}{\pi}\frac{\phi}{b^2+b^3} \stackrel{!}{=} \text{const.}, \tag{8}$$

following from Eq. (4) for the master curve $\zeta(\overline{v})$, which is uniquely determined by the pair potential. Assuming now that bath particles mutually interact as hard spheres, equal in size to their hydrodynamic diameter $b$, density-induced correlations will scale with volume fraction $\phi$. That is to say, the first higher-order correction to Eq. (5) due to correlations is $\mathcal{O}(\phi)$ and thus always vanishes for sufficiently small $\phi$. According to Eq. (8), any particular microrheological scenario can actually be realized at arbitrarily low-volume fractions $\phi$, so long as the relative size of the bath particles $b$ is lowered accordingly.

These considerations can be condensed into a dynamical phase diagram in terms of $\phi$ and $b$ shown in Fig. 4. Notably, the unstable regime, here delineated for the LJ potential with $\epsilon = 5$ and $\sigma = 1$, persists to arbitrarily low volume-fractions $\phi$. The part of the unstable regime where the bath can actually be considered dilute (in $\phi$) is delineated by the shaded area in Fig. 4. In contrast to the sharp crossover from the stable to the unstable region, however, there seems to be no exact threshold in $\phi$ below which volume-exclusion effects become negligible. In order to give an estimate as to viable values of $\phi$, for which the instability is preserved even for hard-sphere bath particles, we have to take into account the strong local aggregation induced by the attractive probe-bath potential. The pair distributions $g(\mathbf{r})$ depicted in Figs. 1(a)–1(d) show that the bath density reaches up to 100-times its bulk value locally. A

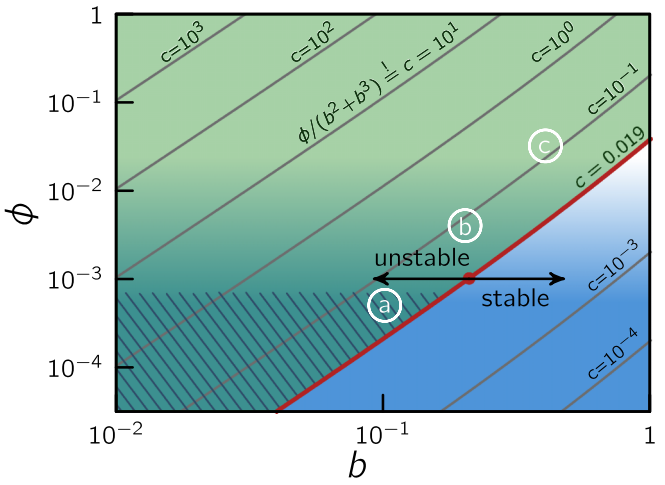


FIG. 4. Mapping of dynamically stable and unstable regimes in terms of volume-fraction $\phi$ and relative bath diameter $b$. Along $\phi/(b^2+b^3) = c = \text{const}$ (thin lines), the microrheological flow curves are invariant. The thick line (red line) demarcates the two regimes, here for a Lennard-Jones potential with $\sigma = 1$ and $\varepsilon = 5$. The shaded area corresponds to the region that is unstable *and* dilute ($\phi \ll 1$), where the pair approximation becomes valid even for a hard-sphere bath. Letters (a)–(c) indicate the state points shown in Figs. 3(a)–3(c) *at constant density* $\rho = 0.92$, with $b$ equal to the effective hard-sphere diameter $b_{\mathrm{BH}}$ of the bath particles and $\phi$ calculated accordingly.

reasonable value for which the bulk of a hard-sphere bath would be considered dilute is $\phi \sim 0.01$. Further demanding that even the local volume-fraction $\phi g(\mathbf{r})$ never exceeds this upper bound, we arrive at a value of $\phi \sim 10^{-4}$. At this volume fraction, according to Fig. 4 the system becomes unstable for bath diameters below $b \sim 10^{-1}$. This claim is supported by the simulation data from Figs. 3(a)–3(c), which are localized in the phase diagram Fig. 4 by the encircled letters. To this end, the hydrodynamic diameter $b$ has been mapped onto to the effective hard-sphere diameter $b_{\mathrm{BH}}$ calculated according to the Barker-Henderson mapping [31],

$$b_{\mathrm{BH}} \equiv 2\int_0^\infty \mathrm{d}r[1 - \mathrm{e}^{-u_b(r)}]. \tag{9}$$

The case in Fig. 3(a) with $\sigma_b = 0.05$ can be mapped onto $b_{\mathrm{BH}} = 0.102$ and $\phi_{\mathrm{BH}} = 5.0 \times 10^{-4}$, supporting the validity of the values estimated above. And indeed, the ideal bath results including the instability are reproduced reasonably well.

### C. Asakura-Oosawa depletion attraction

As an alternative, physically more viable case of colloidal interactions, we consider the well-known Asakura-Oosawa (AO) model [32,33], which deals with the effective attraction between colloids that are suspended among smaller depletants, e.g., polymer coils. While the Lennard-Jones potential has proven very ostensive in the exposition of the microstructural mechanisms underlying the dynamical instability, the gains from an analysis of the AO-potential are threefold: It is an attractive potential that is actually relevant in the colloidal context, giving the parameters explicit physical meaning. Also, extending our analysis to another qualitatively quite different potential supports the claim that the existence of a microrheological instability is a rather generic feature of sufficiently strong attractive probes and hence independent of any particular shape or extension of $u(r)$. Finally, as a hybrid potential it comprises both colloidal volume exclusion and a short ranged continuous attraction. Consequently, the attractive part of the potential given in Eq. (10) with its finite energy scale becomes negligible over the singular repulsion in the strong-driving limit, allowing us to recover the limiting hard-sphere behavior.

The following results are all based on an evaluation of the pair-Smoluchowski Eq. (5) involving the pair potential,

$$u_{\mathrm{AO}} = \begin{cases} \infty, & r < \sigma_c \\ -\eta_p^r(1+q^{-1})^3\left[1 - \frac{3r/\sigma_c}{2(1+q)} + \frac{(r/\sigma_c)^3}{2(1+q)^3}\right], & \\ \qquad \sigma_c < r \leqslant \sigma_c(1+q) & \\ 0, & r \geqslant \sigma_c(1+q), \end{cases} \tag{10}$$

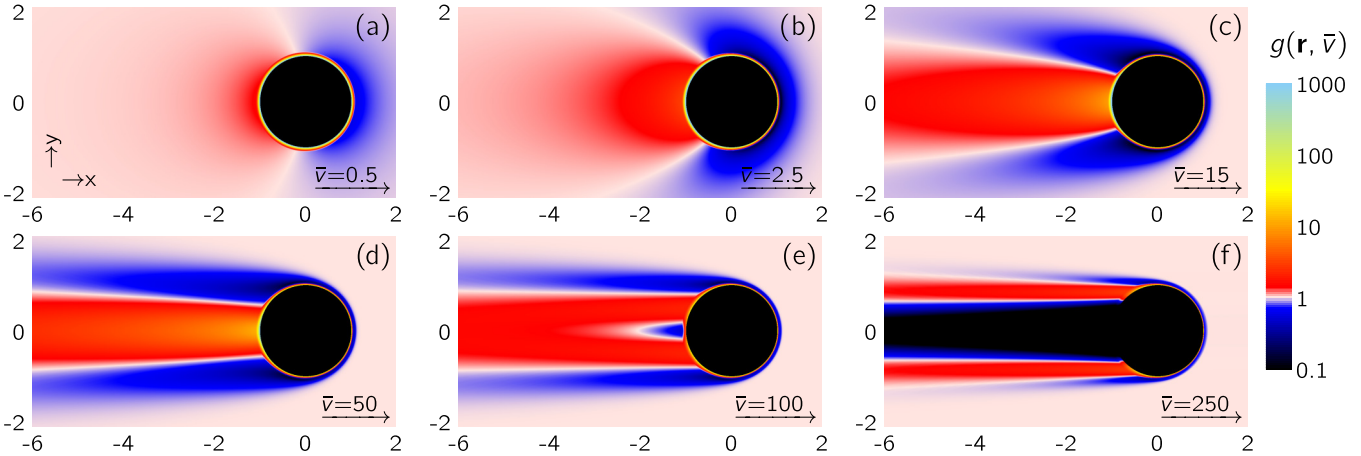


FIG. 5. (a–f) Microstructural deformation around the moving probe in terms of the conditional probability $g(\mathbf{r};\overline{v})$ in the $x$-$y$ plane parameterized by the mean probe velocity $\overline{v}$. Probe and bath particles interact via the AO depletion-attraction potential $u_{\mathrm{AO}}(r)$ with a polymer reservoir packing-fraction $\eta_p^r = 0.5$ and polymer-colloid size ratio $q = 0.10$.

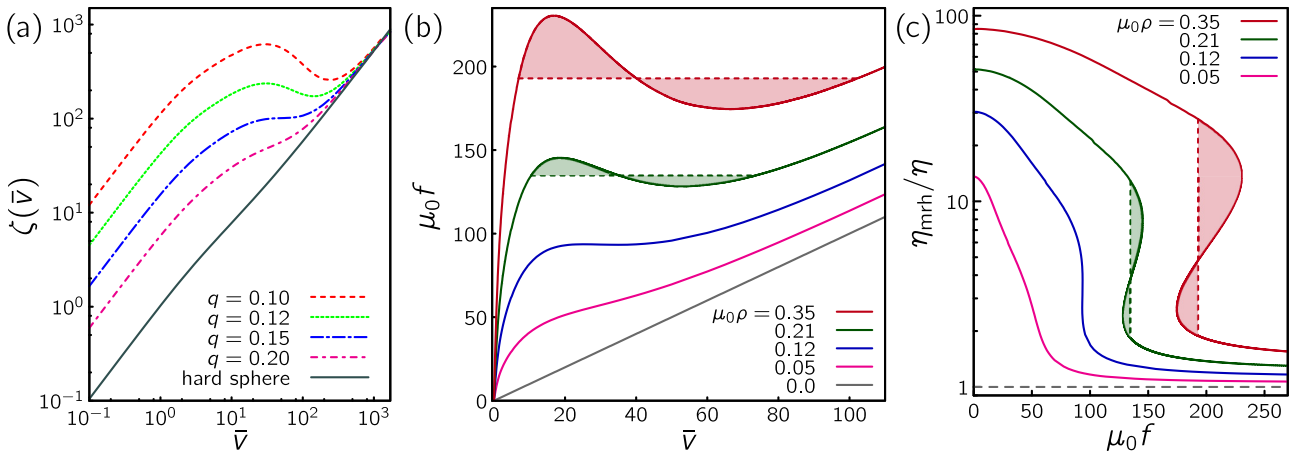


FIG. 6. (a) Master-curves $\zeta(\overline{v})$ for the AO-model with polymer packing-fraction $\eta_p^r = 0.5$ and varying polymer-colloid size ratios $q$ (dashed lines) complemented by the hard-sphere case (solid line) corresponding to $\eta_p^r = 0$. (b) Velocity-force relations $\mu_0 f(\overline{v})$ based on the master-curve $\zeta(\overline{v})$ (solid lines) at $\eta_p^r = 0.5$, $q = 0.10$ for ascending values of $\mu_0\rho$ (bottom to top). Dashed lines represent Maxwell constructions across unstable ranges. (c) Relative microviscosity $\eta_{\mathrm{mrh}}/\eta = \mu_0 f/\overline{v}$ as a function of force $f$ for the same values of $\mu_0\rho$ used in (b). Dashed lines indicate discontinuous transition according to Maxwell construction.

acting between probe and bath particles. The attractive part is a potential of mean force resulting from entropic depletion forces. Here, $\eta_p^r$ is the reservoir packing-fraction of the depletant polymers and $q = \sigma_p/\sigma_c$ is the polymer-colloid size ratio. For the AO-model to hold, this ratio ought to be sufficiently small [33], explicitly $q < 0.155$.

Figures 5(a)–5(f) contain the conditional probabilities $g(\mathbf{r};\overline{v})$ of finding a bath particle around the probe moving with different mean velocities $\overline{v}$. The AO potential is highly attractive only in a narrow perimeter around the hard-sphere exclusion zone, inducing strong local aggregation of bath particles with relative values of $\max\{g(\mathbf{r})\} \sim 1000$ for small $\overline{v}$ [Fig. 5(a)]. The linear-response regime $\overline{v} \lesssim 1$ is characterized by a dipolar excursion from the isotropic equilibrium distribution $g_{\mathrm{eq}}(r) = \exp[-u_{\mathrm{AO}}(r)]$, in agreement with the hard-sphere case. In the nonlinear regime, i.e., $\overline{v} > 1$, the microstructure becomes highly nontrivial. Analogous to the Lennard-Jones potential, increasing advection first pushes the aggregation zone behind the probe, Figs. 5(b)–5(d), and finally flushes it out of the potential well entirely, leaving behind a more or less evacuated wake Figs. 5(e) and 5(f). We recognize this as the mechanism responsible for the instability.

The hard-sphere case, which corresponds to $\eta_p^r = 0$ in terms of the AO model, is recovered for $\overline{v} \to \infty$. Accordingly, the master-curves $\zeta(\overline{v})$, depicted in Fig. 6(a) for hard-spheres along with the AO-model, converge for large $\overline{v}$. Moreover, it can clearly be seen that the unstable behavior is predicated on a certain attraction-strength threshold, here specifically $\eta_p^r = 0.5$ and $q \simeq 0.15$, above which $\zeta(\overline{v})$ becomes nonmonotonous. Only then is it possible to have a likewise unstable velocity-force relation $\mu_0 f = \overline{v} + \mu_0\rho\zeta(\overline{v})$, provided a sufficiently high value of $\mu_0\rho$. In Fig. 6(b), the flow curves are shown for $\eta_p^r = 0.5$, $q = 0.10$ and ascending values of $\mu_0\rho$. The threshold $\mu_0\rho \simeq 0.12$, above which unstable behavior sets in, corresponds to a value of $c = 0.063$ pertaining to the dynamical phase diagram in Fig. 4. The unstable part of the flow curves has again been augmented by an equal-area Maxwell construction to restore invertibility. Finally, the microrheological behavior is shown in terms of the relative microviscosity $\eta_{\mathrm{mrh}}/\eta$ in Fig. 6(c). Here, the dashed lines mark the force at which the discontinuous jump in the microviscosity is to be expected according to the Maxwell construction.

We have thus recovered the unstable microrheological behavior in good qualitative agreement with the Lennard-Jones case, confirming the generality of our central results with regard to different forms of attractive potentials. Being well-studied and experimentally verified, the AO model could serve as a stepping stone towards realistic attractive potentials of the kind needed to bring about the instability. The fact that it involves two parameters that have a distinct physical basis while being independently tunable clearly is an asset in an attempt to find experimentally plausible scenarios. Lower polymer packing fractions $\eta_p^r$ can well suffice to bring about the instability so long as the colloid-polymer size ratio $q$ is adjusted adequately. A caveat remains in that the AO model is based on an equilibrium coarse-graining with respect to the polymer configurations and consequently might break down under nonequilibrium conditions [34]. Generally, effective colloidal forces under flow are nonconservative and hence cannot be represented by a pair potential. While for the particular case of two colloids moving in tandem through a suspension of smaller depletants, such force fields have been studied both theoretically [34–36] and experimentally [37,38]; a similar calculation for the system at hand constitutes a nontrivial task that would merit a future study.

## IV. CONCLUSIONS

We have combined an extension of the simple paradigm with simulations in order to demonstrate both the existence and origin of discontinuous thinning of a soft environment in response to a driven attractive probe. The underlying mechanism rests on the aggregation of the host medium in the potential well and thus depends primarily on attraction strength. Specific details of the pair potential, however, are not essential to the phenomenon itself. This claim has been

substantiated by analyzing the effect for two alternative types of attractive interaction, a Lennard-Jones potential as well as Asakura-Oosawa depletion attraction. Considering a structureless medium has allowed us to clearly expose the principal physical contributions. While simulations involving a (nearly) hard-sphere colloidal bath have revealed that the instability is highly sensitive to density-induced bath correlations, we were able to point out a physically relevant parameter range in terms of volume fraction $\phi$ and relative particle size $b$ wherein our results remain valid even in the case of strongly interacting bath particles. Higher-order corrections to the pair approximation could be incorporated using, e.g., a DFT-like approach [39,40] in the closure of the Smoluchowski Eq. (2). On the practical side, our results show the importance of carefully taking into account the interactions between probe and medium in interpreting experimental data obtained through active microrheology in terms of simple theoretical models. They should also be relevant to predict the response of, e.g., self-propelled colloidal particles in sticky viscoelastic environments [41].

## ACKNOWLEDGMENTS

We acknowledge financial support by the DFG (Grants No. SE1119/3-2 and No. SP1382/1-2).

[1] T. M. Squires and T. G. Mason, Ann. Rev. Fluid Mech. **42**, 413 (2010).
[2] L. G. Wilson and W. C. K. Poon, Phys. Chem. Chem. Phys. **13**, 10617 (2011).
[3] A. M. Puertas and T. Voigtmann, J. Phys.: Cond. Mat. **26**, 243101 (2014).
[4] P. Habdas, D. Schaar, A. C. Levitt, and E. R. Weeks, Europhys. Lett. **67**, 477 (2004).
[5] L. G. Wilson, A. W. Harrison, A. B. Schofield, J. Arlt, and W. C. K. Poon, J. Phys. Chem. B **113**, 3806 (2009).
[6] R. P. A. Dullens and C. Bechinger, Phys. Rev. Lett. **107**, 138301 (2011).
[7] R. Weeber and J. Harting, Phys. Rev. E **86**, 057302 (2012).
[8] D. Mizuno, D. A. Head, F. C. MacKintosh, and C. F. Schmidt, Macromolecules **41**, 7194 (2008).
[9] C. Wilhelm, Phys. Rev. Lett. **101**, 028101 (2008).
[10] S. Choi, S. Steltenkamp, J. Zasadzinski, and T. Squires, Nat. Commun. **2**, 312 (2011).
[11] R. L. Jack, D. Kelsey, J. P. Garrahan, and D. Chandler, Phys. Rev. E **78**, 011506 (2008).
[12] I. Gazuz, A. M. Puertas, T. Voigtmann, and M. Fuchs, Phys. Rev. Lett. **102**, 248302 (2009).
[13] D. Winter, J. Horbach, P. Virnau, and K. Binder, Phys. Rev. Lett. **108**, 028303 (2012).
[14] C. F. E. Schroer and A. Heuer, Phys. Rev. Lett. **110**, 067801 (2013).
[15] O. Bénichou, A. Bodrova, D. Chakraborty, P. Illien, A. Law, C. Mejía-Monasterio, G. Oshanin, and R. Voituriez, Phys. Rev. Lett. **111**, 260601 (2013).
[16] T. M. Squires and J. F. Brady, Phys. Fluids **17**, 073101 (2005).
[17] I. C. Carpen and J. F. Brady, J. Rheol. **49**, 1483 (2005).
[18] R. N. Zia and J. F. Brady, J. Rheol. **57**, 457 (2013).
[19] J. R. Gomez-Solano and C. Bechinger, New J. Phys. **17**, 103032 (2015).
[20] J. R. Gomez-Solano and C. Bechinger, Europhys. Lett. **108**, 54008 (2014).
[21] T. Wang and M. Sperl, Phys. Rev. E **93**, 022606 (2016).
[22] E. Brown and H. M. Jaeger, Rep. Prog. Phys. **77**, 046602 (2014).
[23] R. Seto, R. Mari, J. F. Morris, and M. M. Denn, Phys. Rev. Lett. **111**, 218301 (2013).
[24] M. Wyart and M. E. Cates, Phys. Rev. Lett. **112**, 098302 (2014).
[25] A. Fall, F. Bertrand, D. Hautemayou, C. Mezière, P. Moucheront, A. Lemaître, and G. Ovarlez, Phys. Rev. Lett. **114**, 098301 (2015).
[26] L. B. Chen and C. F. Zukoski, Phys. Rev. Lett. **65**, 44 (1990).
[27] A. A. Rigos and G. Wilemski, J. Phys. Chem. **96**, 3981 (1992).
[28] A. A. Louis, P. G. Bolhuis, J. P. Hansen, and E. J. Meijer, Phys. Rev. Lett. **85**, 2522 (2000).
[29] J. K. G. Dhont, Phys. Rev. E **60**, 4534 (1999).
[30] K. Martens, L. Bocquet, and J.-L. Barrat, Soft Matter **8**, 4197 (2012).
[31] J. A. Barker and D. Henderson, J. Chem. Phys. **47**, 4714 (1967).
[32] S. Asakura and F. Oosawa, J. Chem. Phys. **22**, 1255 (1954).
[33] K. Binder, P. Virnau, and A. Statt, J. Chem. Phys. **141**, 140901 (2014).
[34] J. Dzubiella, H. Löwen, and C. N. Likos, Phys. Rev. Lett. **91**, 248301 (2003).
[35] A. S. Khair and J. F. Brady, P. Roy. Soc. Lond. A Mat. **463**, 223 (2007).
[36] C. Mejia-Monasterio and G. Oshanin, Soft Matter **7**, 993 (2011).
[37] I. Sriram and E. M. Furst, Soft Matter **8**, 3335 (2012).
[38] I. Sriram and E. M. Furst, Phys. Rev. E **91**, 042303 (2015).
[39] J. Reinhardt, F. Weysser, and J. M. Brader, Europhys. Lett. **102**, 28011 (2013).
[40] J. Reinhardt, A. Scacchi, and J. M. Brader, J. Chem. Phys. **140**, 144901 (2014).
[41] J. R. Gomez-Solano, A. Blokhuis, and C. Bechinger, Phys. Rev. Lett. **116**, 138301 (2016).